SCIENCE CHINA
Technological Sciences

Progress of Projects Supported by NSFC

September 2013 Vol.56 No.9: 2207–2218
doi: 10.1007/s11431-013-5315-1

Physical and numerical investigation on transient cavitating flows

HUANG Biao*, WANG GuoYu, ZHAO Yu & WU Qin

School of Vehicle and Transportation Engineering, Beijing Institute of Technology, Beijing 100081, China

Received May 22, 2013; accepted July 16, 2013

The objective of this paper is to investigate transient cavitating flows around a hydrofoil via combined physical and numerical studies. The aims are to 1) investigate the periodic formation, breakup, shedding, and collapse of the sheet/cloud cavities, 2) provide a better insight in the physical mechanism that governs the dynamics and structures of the sheet/cloud cavitation, 3) quantify the influence of cavitation on the surrounding flow structures. Results are presented for a Clark-Y hydrofoil fixed at an angle of attack of α=8° at a moderate Reynolds number, Re=7×10^5, for sheet/cloud cavitating conditions. The experimental studies were conducted in a cavitation tunnel at Beijing Institute of Technology, China. The numerical simulations are performed by solving the incompressible, multiphase unsteady Reynolds-averaged Navier-Stokes (URANS) equations via the commercial code CFX using a transport equation-based cavitation model; a filter-based density corrected model (FBDCM) is used to regulate the turbulent eddy viscosity in both the cavitation regions near the foil and in the wake. The results show that numerical predictions are capable of capturing the initiation of the cavity, growth toward the trailing edge, and subsequent shedding in accordance with the quantitative features observed in the experiment. Regarding vapor shedding in the cavitating flow around the three-dimensional foil, it is primarily attributed to the effect of the re-entrant flow, which is formed due to the strong adverse pressure gradient. The results show strong correlation between the cavity and vorticity structures, demonstrating that the inception, growth, shedding, and collapse of sheet/cloud cavities are important mechanisms for vorticity production and modification.

unsteady cavitating flows, cavity shedding, baroclinic torque, vortex structures

Citation: Huang B, Wang G Y, Zhao Y, et al. Physical and numerical investigation on transient cavitating flows. Sci China Tech Sci, 2013, 56: 2207–2218, doi: 10.1007/s11431-013-5315-1

1 Introduction

In liquid flows, cavitation occurs if the local pressure drops below the saturated vapor pressure, which leads to the formation of vaporous bubbles to relieve the negative pressure [1]. The occurrence of unsteady cavitation in marine propulsion devices such as hydrofoils, propellers, and waterjets can lead to problems such as sudden changes in loads, pressure pulsation, vibrations and noise. Moreover, unsteady cavitation is usually the primary physical phenomenon behind performance alterations in hydraulic machinery [2–4]. For this reason, it is crucial to be able to accurately predict the development, evolution of cavitation, and the resultant impact on the performance. The unsteady behavior of cavitating flows and cavity shedding attract much attention since they seriously affect the hydrodynamic performance of blades and propellers.

To improve the understanding of complex unsteady structures of cavitating flows, various experimental studies have been conducted. Cavitation is highly turbulent and unsteady, the unsteadiness and turbulence interactions have been experimentally investigated in multiple researches. The unsteady structure of cloud cavitation can occur even when the hydrofoil is stationary and inlet is steady [5]. Two

---

*Corresponding author (email: huangbiao@bit.edu.cn) main classes of instabilities of unsteady cavitating flows have been distinguished, intrinsic instabilities and system instabilities, according to the origin of the unsteadiness. In the case of system instability, the unsteady behavior comes from the interaction between the cavity and the rest of the system [6]. For cloud cavitation, the re-entrant jet is rushed from the trailing edge to the leading edge of the sheet cavity, the re-entrant jet after the closure region is the basic mechanism that triggers the shedding of the cloud cavitation [7]. Furthermore, the cavitation instability induced by the development of a re-entrant jet for water past a back step channel was also studied.

It is known that cavitation often involves complex interactions between turbulent flow structures and phase-change dynamics with large variations in fluid density and pressure fluctuations. These physical mechanisms are still not well understood because of the complex, multi-scale, multiphase phenomenon. In the numerical modeling of cavitating flows, the selection of cavitation models plays a major role in the predictions of the onset, growth, break-up, and collapse of cavitation bubbles. In recent years, significant efforts have been made in the development of cavitation models; examples of recent reviewed articles can be found in refs. [8–11]. Most cavitation models assume the flow to be homogenous and isothermal, and apply either a barotropic equation of state or a transport equation to solve for the variation of the mixture density. In barotropic cavitation models, the local mixture density (ρ_m) is assumed to depend only on the local pressure: $\rho_m=(f(p))$. Examples of barotropic cavitation models include those proposed by Chen and Heister [12], and Delannoy and Kueny [13]. A recent experimental finding by Gopalan and Katz [14] has shown that vorticity production is an important aspect of cavitating flows, especially in the cavity closure region. Specifically, this vorticity production is a consequence of the baroclinic torque. Clearly, if a barotropic equation of state is used, the gradients of density and pressure are parallel, which leads to zero baroclinic torque. Hence, barotropic cavitation models will not be able to properly predict the dynamics of cavitating flows, particularly for cases with unsteady cavitation because of the importance of cavitation for vorticity production. So, the transport equation models (TEMs), which solve an additional transport equation for either the mass or volume fraction of vapor, with appropriate source/sink term(s) to regulate the mass transfer between the liquid and vapor phases.

In the numerical modeling of cavitating flows, the selection of turbulence models play an important role in the prediction of the unsteady behavior of cavitating flows. Most unsteady Reynolds-averaged Navier-Stokes (URANS) turbulence models were initially developed for single phase, fully incompressible fluids. Hence, it is not suitable for compressible two-phase mixture flows. To account for the large density jump caused by cavitation, Reboud et al. [15] and Coutier-Delgosha et al. [16] modified the turbulent eddy viscosity of the k-ε RNG URANS model to simulate unsteady cloud cavity in a Venturi-type duct. They found that the URANS model with the modified turbulent eddy viscosity was able to better predict the unsteady re-entrant jet and the shedding of the vapor cloud; however, they also reported that the model was not able to accurately predict the cavity length and shedding frequency for cases with low cavitation numbers. In order to better capture the transient turbulence structures, a large eddy simulation (LES) model was used to simulate sheet/cloud cavitation on a NACA-0015 hydrofoil [17]; they found that it is fundamentally difficult to find a grid independent LES solution unless one explicitly assigns a filter scale. Johansen et al. [18] formulated a filter-based model (FBM) as a compromise between RANS and LES. Wu et al. [19] assessed the validity of FBM turbulence model through unsteady simulations of different geometries, including a square cylinder, a convergent-divergent nozzle, a Clark-Y hydrofoil, and a hollow-jet valve. They found that the FBM is able to better capture the unsteady features than standard RANS models. Kim and Brewton [20] compared numerical predictions with RANS, LES, and RANS/LES hybrid approaches for sheet/cloud cavitation, and found that both LES and hybrid RANS/LES results closely reproduced the salient features such as the breakup of the sheet cavity by the re-entrant jet, and the formation and collapse of the cloud cavity.

Cavitation has been extensively investigated for the past on two-dimensional hydrofoil, however, the cavitation on two-dimensional hydrofoils always displays some 3D effects [21, 22], Satio et al. [23] simulated three-dimensional unsteady cavitating flow around a NACA0015 hydrofoil, and the mechanism of U-shaped cloud cavity formation was clarified. Luo and Ji et al. [24, 25] proposed that regarding vapor shedding in the cavitating flow around three-dimensional foils, it is primarily attributed to the effect of the re-entrant flow consisting of a re-entrant jet and a pair of side-entrant jets. The objective of this paper is to investigate transient cavitating flows around 3D hydrofoil via combined physical and numerical studies. We will investigate the unsteady cavitating structures, including the periodic formation, breakup, shedding, and collapse of the sheet/cloud cavities, provide a better insight in the physical mechanism that governs the dynamics and structures of the sheet/cloud cavitation, and quantify the influence of cavitation on the surrounding flow structures.

The numerical models are presented in Section 2. Summary of the experimental and numerical setup are shown in Sections 3 and 4, respectively. In Section 5, comparisons of numerical predictions with experimental visualizations of global multiphase structures are presented, followed by detailed analysis of the effects of cavitation on the flow structures. Finally, the major findings and future work are summarized in Section 6.

2 Numerical model

2.1 Conservation of mass & momentum

The URANS equations, in their conservative form, for a Newtonian fluid without body forces and heat transfers are presented below along with the mass transport equation in the Cartesian coordinates:

$$\frac{\partial \rho_{\mathrm{m}}}{\partial t}+\frac{\partial(\rho_{\mathrm{m}} u_j)}{\partial x_j}=0, \tag{1}$$

$$\frac{\partial(\rho_{\mathrm{m}} u_i)}{\partial t}+\frac{\partial(\rho_{\mathrm{m}} u_i u_j)}{\partial x_j}=-\frac{\partial p}{\partial x_i}+\frac{\partial}{\partial x_j}\left[(\mu_{\mathrm{m}}+\mu_{\mathrm{T}})\left(\frac{\partial u_i}{\partial x_j}+\frac{\partial u_j}{\partial x_i}-\frac{2}{3}\frac{\partial u_k}{\partial x_k}\delta_{ij}\right)\right], \tag{2}$$

$$\frac{\partial \rho_{\mathrm{l}}\alpha_{\mathrm{l}}}{\partial t}+\frac{\partial(\rho_{\mathrm{l}}\alpha_{\mathrm{l}} u_j)}{\partial x_j}=\dot{m}^{+}+\dot{m}^{-}, \tag{3}$$

$$\rho_{\mathrm{m}}=\rho_{\mathrm{l}}\alpha_{\mathrm{l}}+\rho_{\mathrm{v}}\alpha_{\mathrm{v}}, \tag{4}$$

$$\mu_{\mathrm{m}}=\mu_{\mathrm{l}}\alpha_{\mathrm{l}}+\mu_{\mathrm{v}}\alpha_{\mathrm{v}}, \tag{5}$$

where ρ_{m} is the mixture density, ρ_{l} is the liquid density, ρ_{v} is the vapor density, α_{v} is the vapor fraction, α_{l} is the liquid fraction, u is the velocity, p is the pressure, μ_{m} is the mixture laminar viscosity, μ_{l} and μ_{v} are respectively the liquid and vapor dynamic viscosities, and μ_{T} is the turbulent viscosity. The subscripts (i, j, k) denote the directions of the Cartesian coordinates. The source ($\dot{m}^{+}$) and sink ($\dot{m}^{-}$) terms in eq. (3) represent the condensation and evaporation rates, respectively, as will be discussed below.

2.2 Cavitation model

The Kubota model [2] is a transport-equation based cavitation model that assumes a constant nuclei size and nuclei density in the fluid domain. The growth and collapse of the bubble clusters are assumed to be governed by the simplified Rayleigh-Plesset equation [2]. The cavitation process is governed by the mass transfer equation given in eq. (3), and the source and sink terms are defined as follows:

$$\dot{m}^{-}=-C_{\mathrm{dest}}\frac{3\alpha_{\mathrm{nuc}}(1-\alpha_{\mathrm{v}})\rho_{\mathrm{v}}}{R_{\mathrm{B}}}\left(\frac{2}{3}\frac{p_{\mathrm{v}}-p}{\rho_{\mathrm{l}}}\right)^{1/2},\quad p<p_{\mathrm{v}}, \tag{6}$$

$$\dot{m}^{+}=C_{\mathrm{prod}}\frac{3\alpha_{\mathrm{v}}\rho_{\mathrm{v}}}{R_{\mathrm{B}}}\left(\frac{2}{3}\frac{p-p_{\mathrm{v}}}{\rho_{\mathrm{l}}}\right)^{1/2},\ p>p_{\mathrm{v}}, \tag{7}$$

where α_{nuc} is the nucleation volume fraction, R_{B} is the bubble diameter, p_{v} is the saturated liquid vapor pressure, and p is the local fluid pressure. C_{dest} is the rate constant for vapor generated from the liquid in a region where the local pressure is less than the vapor pressure. Conversely, C_{prod} is the rate constant for re-conversion of vapor back into liquid in regions where the local pressure exceeds the vapor pressure. In this work, the assumed model constants are $\alpha_{\mathrm{nuc}}=5\times10^{-4}$, $R_{\mathrm{B}}=1\times10^{-6}$ m, $C_{\mathrm{dest}}=50$, and $C_{\mathrm{prod}}=0.01$, which are the default values in CFX [26], and are used because of their supposedly general applicability.

It should be noted that eqs. (6) and (7) are different from the original model proposed by Kubota et al. [8], and instead follows the form presented in [26]. Since the evaporation rate is much higher than the condensation rate, different coefficients are needed for condensation and evaporization terms, as shown in eqs. (6) and (7). In addition, α_{v} is replaced by α_{nuc} $(1-\alpha_{\mathrm{v}})$ in the vaporization term to account for the decrease of the nucleation site density with the increase of the vapor volume fraction [26].

2.3 Filter-based density corrected model (FBDCM)

The numerical results shown in this paper are obtained using the commercial CFD code, CFX, to solve the URANS equations using a modified form of the original k-ε turbulence model [27], which was developed for fully incompressible single phase flows. As shown in refs. [15, 16], the original two-equation models may over-predict the turbulent eddy viscosity in the cavitation region and result in over-prediction of the turbulent stresses, causing the re-entrant jet to lose momentum and not be able to cut across the cavity sheet, which significantly modifies the cavity shedding behavior**.**

To improve numerical simulations by taking into account the influence of the local compressibility effect on turbulent closure model, the density corrected model (DCM) proposed by Reboud et al. [15] and Coutier-Delgosha et al. [16] is adopted to reduce the turbulent eddy viscosity based on the local liquid volume fraction α_v in eq. (2) with $\mu_{\mathrm{T\_DCM}}$:

$$\begin{aligned}\mu_{\mathrm{T\_DCM}}&=\frac{C_\mu\rho_{\mathrm{m}}k^2}{\varepsilon}f_{\mathrm{DCM}},\quad C_\mu=0.09,\\ f_{\mathrm{DCM}}&=\frac{\rho_{\mathrm{v}}+(1-\alpha_{\mathrm{v}})^n(\rho_{\mathrm{l}}-\rho_{\mathrm{v}})}{\rho_{\mathrm{v}}+(1-\alpha_{\mathrm{v}})(\rho_{\mathrm{l}}-\rho_{\mathrm{v}})}.\end{aligned} \tag{8}$$

In eq. (8), the parameters, except for the function f_{DCM}, are set to the same values as the original k-ε proposed by Launder and Spalding [27]. Similar modification has also been applied by Ducoin et al. [28] and Huang et al. [29] for prediction of unsteady sheet/cloud cavitation; they showed good agreements with experimental measurements using n=3.

Instead of the DCM model, Johansen et al. [18] proposed a filter-based model (FBM) to help reduce μ_{T}. Specifically, the turbulent eddy viscosity is modified by comparing the local turbulence length scale, $k^{3/2}/\varepsilon$, with the filter size, λ, which is selected based on the local mesh size:

$$\mu_{\mathrm{T\_FBM}} = \frac{C_\mu \rho_\mathrm{m} k^2}{\varepsilon} f_\mathrm{FBM},\ C_\mu = 0.09,\ f_\mathrm{FBM} = \min\left(1, \frac{\lambda \cdot \varepsilon}{k^{3/2}}\right). \quad (9)$$

When the $\lambda >> k^{3/2}/\varepsilon$, e.g., in near-wall region where the local mesh size is much greater than the turbulence length scale, eq. (9) yields $\mu_{\mathrm{T\_FBM}}=C_\mu\rho_\mathrm{m}k^2/\varepsilon$, i.e., the standard k-ε model is recovered. When $\lambda << k^{3/2}/\varepsilon$, e.g., in the region away from the wall where the local mesh size is smaller than the turbulence length scale, $\mu_{\mathrm{T\_FBM}}=C_\mu\rho_\mathrm{m}\lambda k^{1/2}$. The FBM ensures that the turbulent eddy viscosity does not increase beyond the RANS value. In particular, the FBM model will help limit the turbulent eddy viscosity in the cavitating wake, where the DCM is not effective in reducing the turbulent eddy viscosity because of the low vapor fraction in the shed cloud cavity. Hence, the FBM can help improve the prediction of cavitating wake dynamics by allowing the shed cloud cavities to shed and diffuse downstream.

Although both the FBM and DCM approaches are designed to reduce the turbulent eddy viscosity, they act in different regions. The FBM approach mainly modifies the eddy viscosity away from the near-wall region, where the local mesh size is smaller than the turbulent length scale. On the other hand, the DCM approach mainly modifies the turbulent eddy viscosity in the cavitating region with significant density gradient, such as in the cavity closure region near the foil wall. To limit the turbulent eddy viscosity in the cavitation region near the foil wall and in the cavitating wake region, a filter-based density corrected model (FBDCM) that combines the strengths of both the FBM and DCM models is proposed, which replaces μ_T in eq. (2) with $\mu_{\mathrm{T\_hybrid}}$:

$$\begin{aligned} &\mu_{\mathrm{T\_hybrid}} = \frac{C_\mu \rho_\mathrm{m} k^2}{\varepsilon} f_\mathrm{hybrid},\ C_\mu = 0.09, \\ &f_\mathrm{hybrid} = \chi(\rho_\mathrm{m}/\rho_\mathrm{l}) f_\mathrm{FBM} + [1-\chi(\rho_\mathrm{m}/\rho_\mathrm{l})] f_\mathrm{DCM}, \end{aligned} \quad (10)$$

$$\begin{aligned} \chi(\rho_\mathrm{m}/\rho_\mathrm{l}) = {} & 0.5 \\ & + \tanh\left[\frac{C_1(0.6\rho_\mathrm{m}/\rho_\mathrm{l} - C_2)}{0.2(1-2C_2)+C_2}\right] \Big/ [2\tanh(C_2)], \quad (11) \end{aligned}$$

where C_1 and C_2 are chosen to be 4 and 0.2, respectively. The hybrid function χ ($\rho_\mathrm{m}/\rho_\mathrm{l}$) (shown in Figure 1) is used to continuously blend the FBM and DCM based on local mixture density, which will help limit the over-prediction of the turbulent eddy viscosity in the cavitating regions on the foil wall and in the wake. Validation of the FBDCM turbulence model with the assumed constants for the case of unsteady cavitating flow around a same 2D Clark-Y hydrofoil used in this study has been presented in ref. [30].

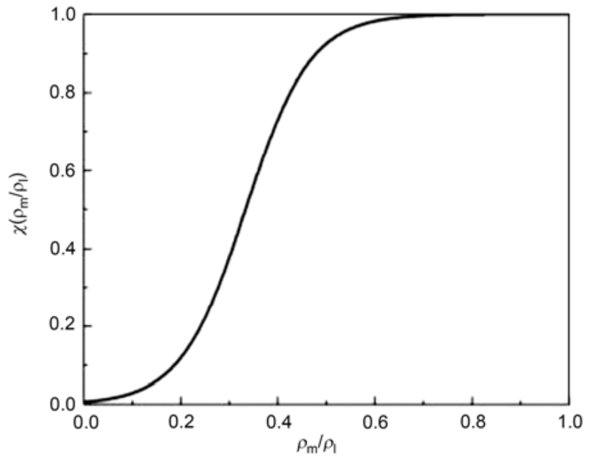

Figure 1 Distribution of hybrid function χ for the FBDCM model according to eq. (11).

3 Experimental setup and description

The numerical predictions in the present study are compared with experimental visualizations and measurements of a Clark-Y hydrofoil conducted at the cavitation tunnel at Beijing Institute of Technology [30, 31]. The test section is 0.133 m^2 squared and 0.7 m long. The cavitation tunnel is capable of generating free stream velocity ranging from 2–15 m/s with a minimum cavitation number of $\sigma=2(p_\infty-p_\mathrm{v})/(\rho_\mathrm{l}U_\infty^2)=0.3$, where p_∞ is the reference static pressure, p_v is the saturated vapor pressure of water, and U_∞ is the free stream velocity. The tunnel inflow turbulence intensity, defined as $U_{\infty\mathrm{rms}}/U_\infty$ at the inlet of the test-section, is about 2%. The foil has a uniform cross-section with a Clark-Y thickness distribution with a maximum thickness-to-chord ratio of 11.7%, the chord length is c=0.07 m, the span length is s=0.07 m. The hydrofoil is mounted horizontally in the tunnel test section at a fixed angle of attack of $\alpha=8^\circ$. In the experiments [30, 31], high-speed video and particle image velocimetry (PIV) technique are used to measure the flow velocity and vorticity fields, as well as cavitation patterns.

4 Numerical setup and description

To investigate the structures of unsteady sheet/cloud cavitating flows via combined physical and numerical analysis, results are shown for the Clark-Y hydrofoil described in Section 3. The results shown in this paper correspond to the hydrofoil fixed at $\alpha=8^\circ$ and subject to a nominal free stream velocity of U_∞=10 m/s, which yields a moderate Reynolds number of $Re=U_\infty c/\nu_\mathrm{l}=7\times10^5$. The density and dynamic viscosity of the liquid are set to be ρ_l=999.19 kg/m^3 and $\mu_\mathrm{l}=\rho_\mathrm{l}\nu_\mathrm{l}=1.139\times10^{-3}$ Pa s, respectively, which correspond to fresh water at 25°C. The vapor density is ρ_v=0.02308 kg/m^3

and the vapor viscosity is μ_v =9.8626×10^{-6} Pa s. The vapor pressure of water at 25°C is p_v=3169 Pa.

The computational domain follows the boundaries of the cavitation tunnel, as shown in Figure 2. A no-slip boundary condition is imposed on the hydrofoil surface, and no-slip symmetry conditions are imposed on the side boundaries of the tunnel. The inlet velocity is set to be U_∞=10 m/s and the outlet pressure is set to vary according to the cavitation number, defined as $\sigma=(p_\infty-p_v)/(0.5\rho_l U_\infty^2)$. A constant turbulent intensity of 2% is set at the inlet boundary and is equal to the experimentally measured mean turbulent intensity.

All cavitating runs have been initialized with steady-state, fully wetted calculations to avoid any vapor fraction at the initial time step. The tunnel pressure is then decreased progressively until the particular cavitation number is reached. The 3D fluid mesh (shown in Figure 2) is composed of 1200000 elements with 80 structured elements across the foil boundary layer, which is selected to ensure $y^+=yu_\tau/\nu_l=1$, where y is the thickness of the first cell from the foil surface, and u_τ is the wall frictional velocity. Mesh refinements are performed at the foil leading edge, trailing edge, and in the wake region. To get better capture of the 3D flow structures, 80 nodes are set along the spanwise directions. The time integration scheme is a second-order backward Euler algorithm, and the spatial derivatives are computed using a second-order upwind scheme. In the computation, $\Delta t=1\times10^{-4}$ s is chosen based on convergence studies, which gives an average CFL number of CFL=$U_\infty\Delta t/\Delta x$=1. In the FBDCM model, the filter size in eq. (9) is chosen to be $\lambda=1.05\Delta_{\max,O}$. Here, $\Delta_{\max,O}$ is the largest grid size of the O shape grid around the hydrofoil in the computation domain, which is around 0.012c, and parameter n is chosen to be 3.

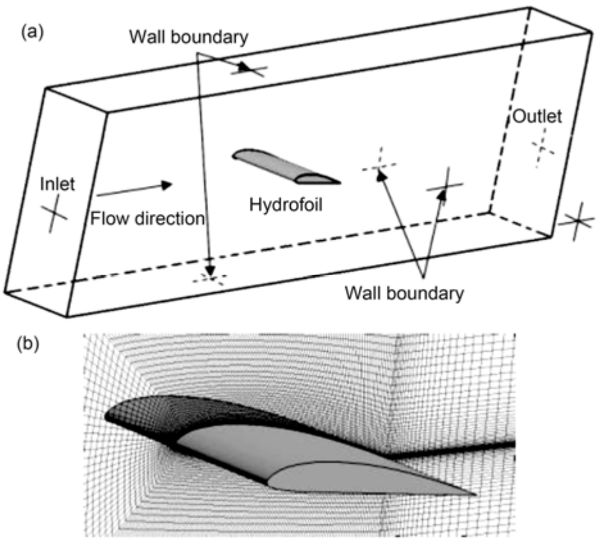

Figure 2 3D computation domain boundary conditions and mesh generation around the hydrofoil surface.

5 Results and discussion

5.1 Global multiphase structures associated with cloud cavitating flows

The unsteady cavitating flows around the Clark-Y hydrofoil are investigated by both experimental and numerical methods to charify the globe multiphase structures. In the present study, when the cavitation number is reduced to σ=0.80, the sheet cavitation grows and the trailing edge becomes increasingly unsteady until the transient cloud cavitation develops. It is observed that cloud cavitation has a distinctly quasi-periodic pattern. Figure 3(a) and (b) show the comparisons of cavitation patterns predicted and observed in the experiment within a single flow cycle, the absolutely pressure contours of the foil surface are also shown in Figure 3(b). In order to better investigate the structure of vortex structure, the iso-surface of the conventional vortex definition criterion, Q, is shown in Figure 3(c). Q is defined as $Q=1/2(|\Omega|^2-|S|^2)$, where Ω is the vorticity tensor, and S is the rate of strain tensor. Comparing Figure 3(b) with (c), it is clear that the shape of the cavitating vortex structure for the Q-criterion is more complicated than that of the vapor fraction iso-surface, which is more consistent with the experiments. The reference period of the cloud cavitation is estimated to be about T_{cycle}=40 ms=5.7c/U_∞ based on both video visualizations and the numerical results.

As shown in Figure 3, the numerical predictions are capable of capturing the initiation of the cavity, growth toward the trailing edge, and subsequent shedding, in accordance with the qualitative features observed in the experiment. At t=0.125T_{ref}, a small partial sheet cavity is formed near the foil leading edge (LE) while the cloud shedding cavity formed from the breakup of the previous sheet cavity is still clearly visible near the foil trailing edge (TE). The stable attached sheet cavity grows to its maximum length at t=0.475T_{ref}, when the cavity interface becomes wavy/bubbly, particularly near the cavity trailing edge, as shown on the middle pictures in Figure 3(3). When the adverse pressure gradient is strong enough to overcome the weaker momentum of the flow confined by the near-wall region, a re-entrant jet forms and pushes the flow toward the foil leading edge, as shown at t=0.625T_{ref} in Figure 3(4). With the development of the re-entrant jet, the interface becomes increasingly unsteady with a bubbly appearance. The development of the re-entrant jet and its impact on the vortex structures and cavity patterns are evident on Figure 3(5) and (6); it should be noted that the vortex structures given by iso-surface of vapor fraction is slightly underestimated. As the re-entrant flow reaches the vicinity of cavity leading edge, the cavity is lifted away from the wall and sheds downstream in the form of cloud cavity, which corresponds to the large-scale vortex structure observed near the foil TE on the right picture in Figure 3(6). These results suggest that

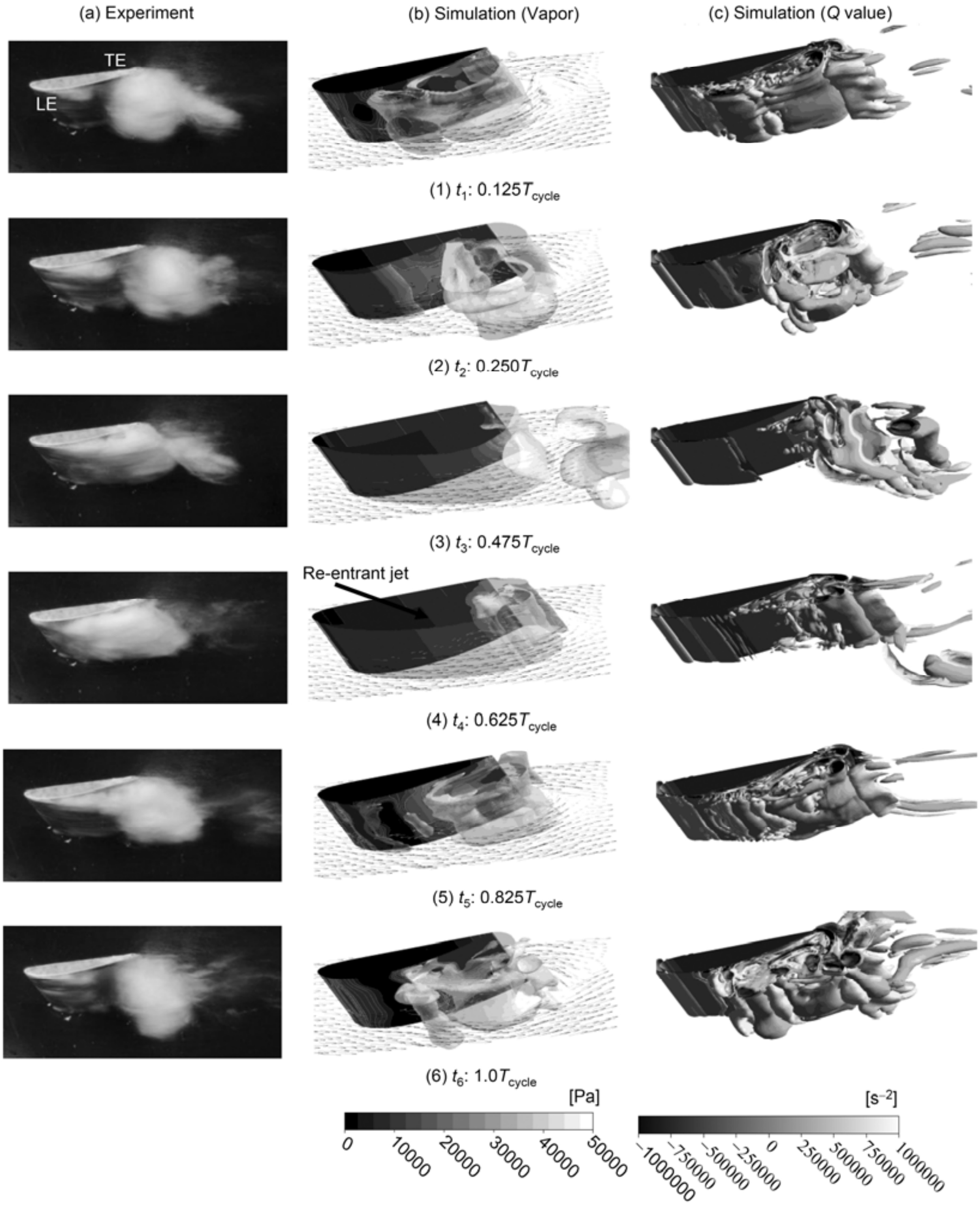

(1) t_1: $0.125T_{\text{cycle}}$

(2) t_2: $0.250T_{\text{cycle}}$

(3) t_3: $0.475T_{\text{cycle}}$

(4) t_4: $0.625T_{\text{cycle}}$

(5) t_5: $0.825T_{\text{cycle}}$

(6) t_6: $1.0T_{\text{cycle}}$

Figure 3 Comparisons of the experimentally observed cavitation pattern (a), numerically predicted vapor fraction iso-surface and flow streamlines (b) and iso-surfaces of the conventional vortex definition criterion Q (c) for $\sigma = 0.80$, $Re=7\times10^5$, $\alpha=8^\circ$. Values of each iso-surface are $Q=4\times10^5$ s^{-2}, 5×10^5 s^{-2}, 6×10^5 s^{-2}, 7×10^5 s^{-2}, 8×10^5 s^{-2}, 9×10^5 s^{-2}, respectively.

the interaction between the circulating flow and the shedding vapor cloud is closely related to the complicate vortex structure.

In order to better understand the physical mechanism that governs the dynamics and structures of the unsteady sheet/cloud cavitating flows, the predicted vapour volume fraction of the cavity as a function of space and time in middle span of the foil is shown in Figure 4(a). The predicted contours of the negative (upstream) axial (u) velocity and relative higher pressure (C_p>0) as a function of space and time are shown in Figures 4(b) and (c), respectively. In Figure 4, $T_0=c/U_\infty$ and $L_0=c$ are the characteristic time and length scales, respectively. The Strouhal number, which characterizes the shedding frequency f, is defined as $St_c=fc/U_\infty=0.185$ based on experimental measurements, and was found to be the same as the one based on the numerical simulation. As seen from Figure 4(a), the cavity shedding process is periodic, and the development of the re-entrant jet is responsible for triggering the cavity detachment, and hence unsteadiness. When the attached cavity begins to grow within a single

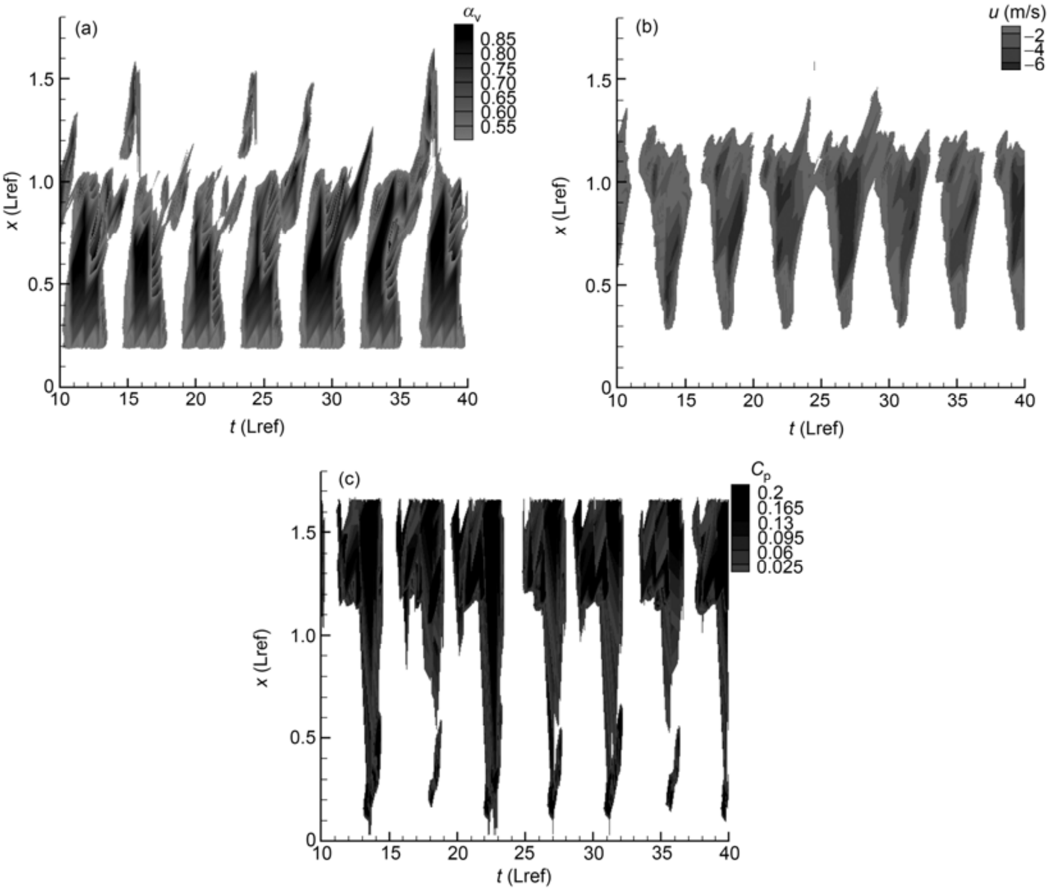

Figure 4 Numerically predicted time evolution of the predicted (a) water vapor fraction (α_v) and (b) reverse u-velocity (c) relative high pressure in various sections (the position is reported in ordinate, from the foil leading edge x/L_0=0 to the trailing edge x/L_0=1) of the middle span of the foil for σ=0.80, Re=7×10^5, α=8°.

flow cycle, there is no reverse flow due to the insignificant adverse pressure gradient that was assumed to be responsible for the jet formation. When the attached cavity grows to its maximum, the sudden increase of the pressure at the trailing edge, as shown in the absolute pressure contours on the foil surface in Figure 4(c), leads to the amplification of the re-entrant jet, and the magnitude of reverse flow can reach $0.6U_\infty$. When the reverse flow reaches the leading edge of the hydrofoil, the cavity is lifted away from the wall and shed downstream in the form of cloud cavitation.

5.2 Unsteady cloud shedding process in the cavitating wake

Recently, with the emergence and popular use of modern high speed camera and particle-imaging techniques, it is possible to explore the detailed structures of the cavity closure region and in the cavitating wake. An important objective of the present experimental study is to improve the understanding of the interactions between cloud cavitation and the turbulent cavitating wake.

Figures 5 and 6 show the comparison of the predicted and experimental evolution of the cloud shedding process. The primary sheet cavity has a bubbly structure because of disturbances caused by the re-entrant jet, which is responsible for the breakup, lift off, and subsequent shedding of a large cloud cavity. Due to the effects of the side-wall, both the experimental and simulation results show that the cloud cavity is distorted into a U-shape vapor structure as it moves downstream, which then splits at its head and finally collapses violently at its legs. Figure 7 shows the absolutely pressure contours of the iso-surface of the vapor fraction, and the development of the high pressure at the head of the U-shape vapor structure is responsible for triggering the cavity splitting, and hence collapsing. The cavity shedding process is very similar to the schematic diagram of typical cloud cavity transformation in ref. [7].

5.3 Influence of cavitation on vorticity field

In order to get a better understanding of the influence of cavitation on the vortex flow structure, Figure 8 shows the side-by-side comparisons of the predicted and measured normalized out-of-plane (z-component) vorticity fields in

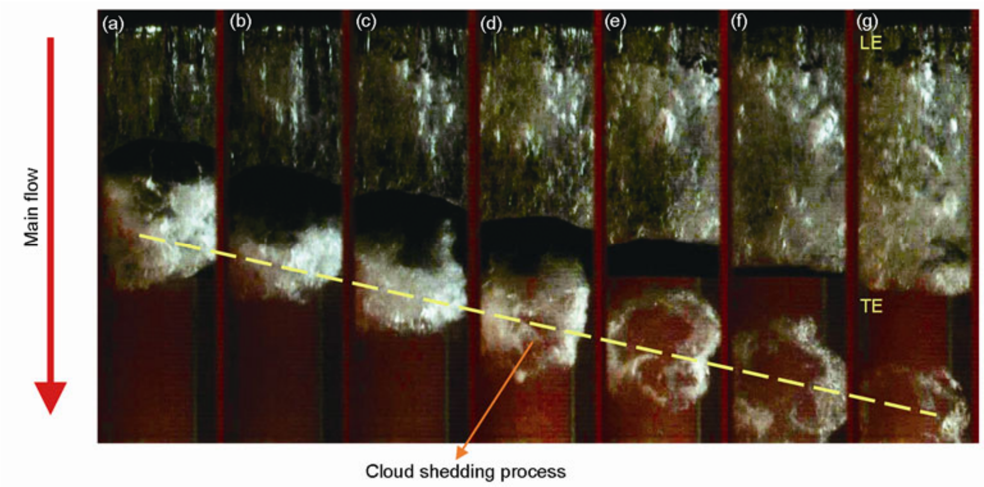

Figure 5 Time sequence of photographs of a cloud cavity obtained via high-speed video at σ=0.80, *Re*=7×10^5, α=8°. (a) 0.375T_{cycle}; (b) 0.400T_{cycle}; (c) 0.425T_{cycle}; (d) 0.450T_{cycle}; (e) 0.475T_{cycle}; (f) 0.500T_{cycle}; (g) 0.525T_{cycle}.

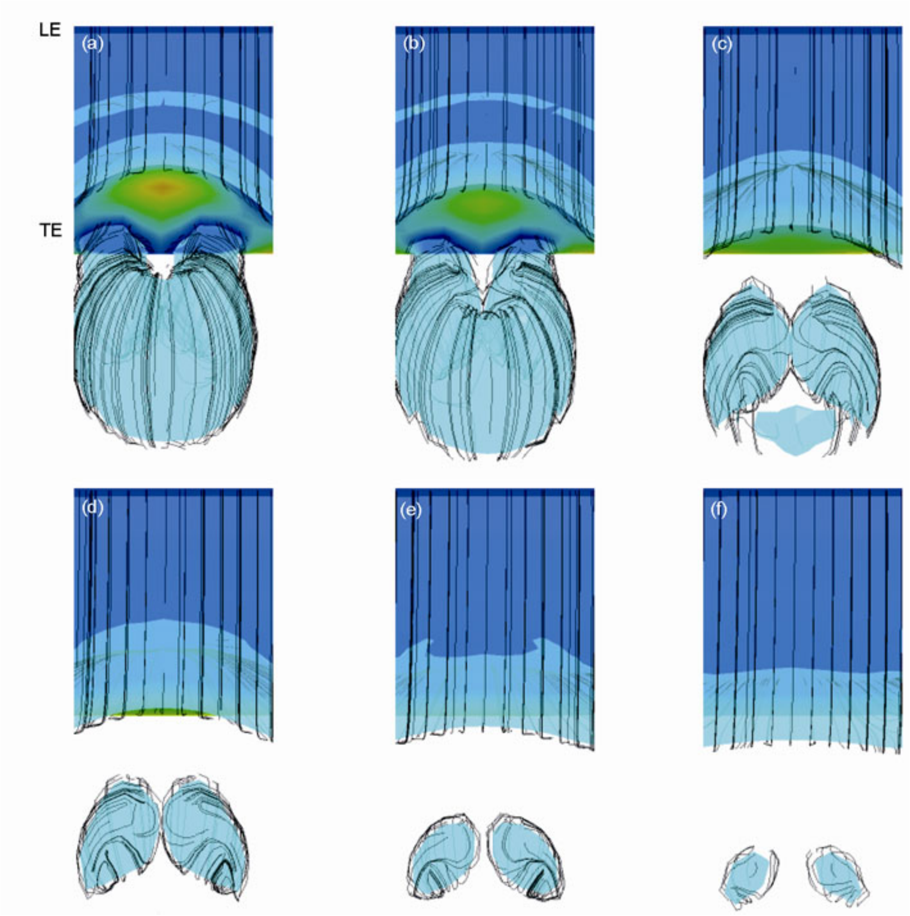

Figure 6 Time sequence of photographs of a cloud cavity (Num) at σ=0.80, *Re*=7×10^5, α=8°. (a) 0.375T_{cycle}; (b) 0.400T_{cycle}; (c) 0.425T_{cycle}; (d) 0.450T_{cycle}; (e) 0.500T_{cycle}; (f) 0.525T_{cycle}.

the middle span of the foil, ω_z/ω_o, for σ=2.00 and 0.80. The detailed comparison of the predicted normalized vorticity profiles with the measured values for σ=2.00 and 0.80 at the selected monitoring locations are shown in Figure 9. Here, ω_z is defined as

$$\omega z = \partial v / \partial x - \partial u / \partial y, \qquad (12)$$

and $\omega_o = \dfrac{U_0}{\delta} \approx 1.43\times10^3\ \text{s}^{-2}$ ($\delta\approx0.1c$=0.007 m is the appro-

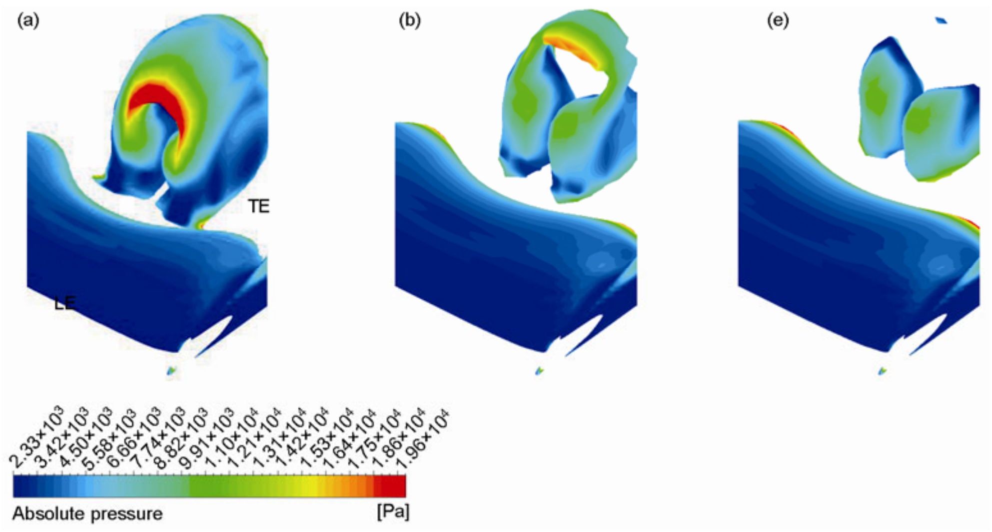

Figure 7 Time sequence of photographs of a cloud cavity (Num) at σ=0.80, *Re*=7×10^5, α=8°. (a) 0.400T_{cycle}; (b) 0.425T_{cycle}; (c) 0.450T_{cycle}.

ximated turbulent boundary layer thickness at the foil trailing edge based on the experimental measurements of the flow velocity for the subcavitating case at σ=2.00). In general, good agreement is observed between the measured and predicted values, especially considering the difficulties in experimental measurements and numerical simulations. However, some differences are observed between the CFD results and experimental data near the cavity closure region.

As shown in Figure 8, for σ=2.00, a counter-clockwise (positive) vortex can be observed at the foil leading edge (LE), and another small counter-clockwise vortex can be observed at the foil trailing edge (TE) from the suction side along with a smaller clockwise (negative) vortex at the foil TE from the pressure side. For σ=0.80, a large-scale counter-clockwise vortex is observed in the cavitating region along with a much stronger clockwise TE vortex than the subcavitating case.

The detailed normalized vorticity profiles shown in Figure 9 for the subcavitating case confirm the existence of a thin vortical layer near the foil surface, and the thickness of the vortical zone grows toward the trailing edge, with a maximum thickness of approximately 0.1*c*. For the sheet/cloud cavitating case, the vortical zone is much thicker (near 0.3*c* at the foil trailing edge), the vorticity profile is drastically different, and the magnitude of the vorticity is much greater than for the subcavitating case. The results shown in Figures 8 and 9 clearly demonstrate that the unsteady sheet/cloud cavity is an important source of vorticity production and modification, which leads to significant increase in the turbulence level and turbulent boundary layer thickness.

As suggested in refs. [14] and [28], the baroclinic torque created by the mixture density and pressure gradients in the cavitating region is responsible for the alteration of the vorticity field, which is evident via the vorticity transport equation:

$$\frac{D\boldsymbol{\omega}}{Dt}=(\boldsymbol{\omega}\cdot\nabla)\boldsymbol{V}-\boldsymbol{\omega}(\nabla\cdot\boldsymbol{V})+\nabla\rho_{\mathrm{m}}\times\nabla p/\rho_{\mathrm{m}}^{2}+(\upsilon_{\mathrm{m}}+\upsilon_{\mathrm{T}})\nabla^{2}\boldsymbol{\omega}, \tag{13}$$

where $\boldsymbol{\omega}$ and $\boldsymbol{V}$ are respectively the fluid vorticity and velocity vectors. υ_{m} is the laminar kinematic viscosity and υ_{T} is the modified turbulent kinematic viscosity.

The first term on the right-hand side (RHS) of eq. (13) is the vortex stretching term. The second term on the RHS is the volumetric expansion/contraction (dilatation) term. The third term on the RHS of corresponds to the generation of vorticity from unequal acceleration caused by unaligned pressure and density gradients, e.g. the generation of a shear layer caused by the faster acceleration of the lighter fluid (vapor) relative to the heavier fluid (water). The fourth term on the RHS represents the laminar and turbulent diffusion of the vorticity.

To examine the influence of cavitation on the production/alteration of vorticity around the cavitating flow, the time evolution of predicted strengths of vortex stretching term $\left|(\boldsymbol{\omega}\cdot\nabla)\boldsymbol{V}\right|$, volumetric expansion/contraction (dilatation) term $\left|\boldsymbol{\omega}(\nabla\cdot\boldsymbol{V})\right|$, baroclinic torque $\left|\nabla\rho_{\mathrm{m}}\times\nabla p/\rho_{\mathrm{m}}^{2}\right|$ and viscoclinic torque $\left|(\upsilon_{\mathrm{m}}+\upsilon_{\mathrm{T}})\nabla^{2}\boldsymbol{\omega}\right|$ for σ=0.80 are shown in Figure 10. The vortex stretching term is highly dependent on the cavitation evolution, and the dilation term ($\nabla\cdot\boldsymbol{V}$) represents the vortex stretching due to the flow compressibility and is not zero for the cavitation region. The baroclinic term modifies the vorticity field in regions with high density and pressure gradients, i.e., along the liquidvapor interface and near the cavity closure. The magnitude of the baroclinic term seems considerable compared to the vortex

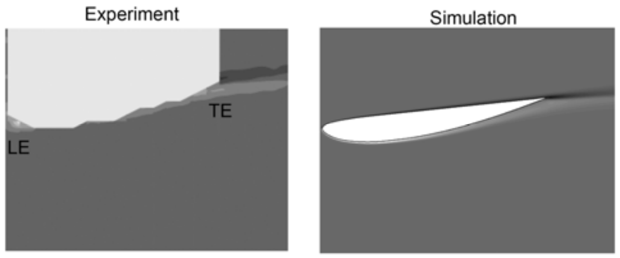

(a) Subcavitation (σ=2.00)

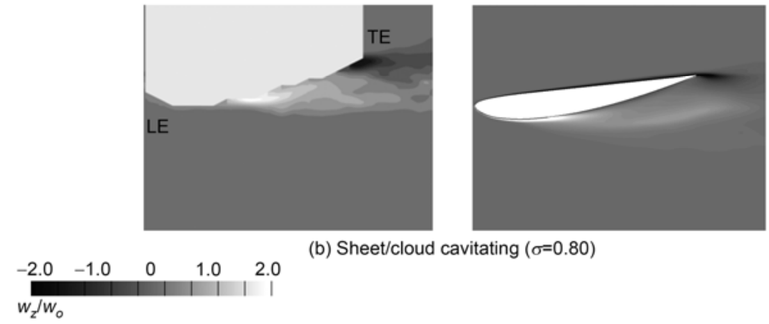

(b) Sheet/cloud cavitating (σ=0.80)

Figure 8 Measured (left) and predicted (right) normalized averaged *z*-vortity, ω_z/ω_o contours (the counter clockwise is positive) on the suction side of the hydrofoil at (a) σ=2.00 and (b) σ=0.80, Re=7×10^5 , α=8°.

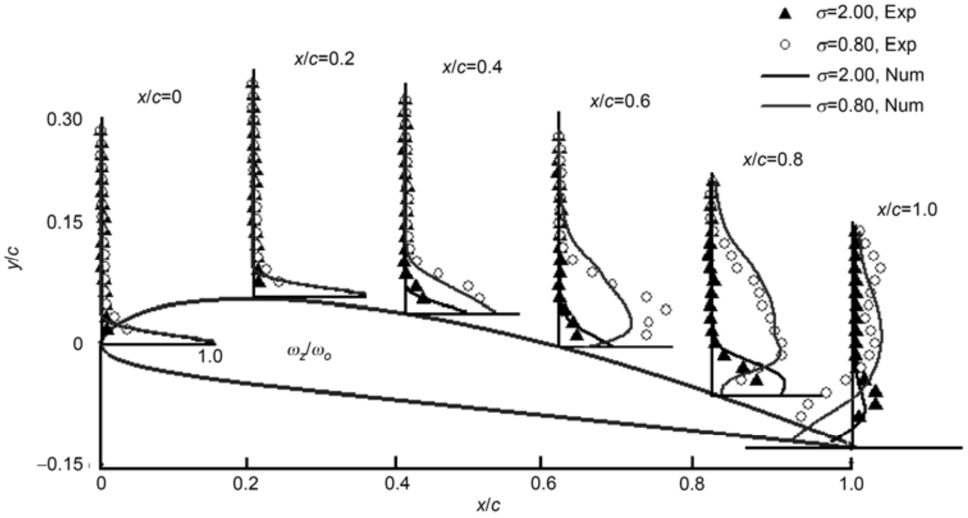

Figure 9 Comparisons of the measured and predicted normalized averaged *z*-vortities, ω_z/ω_o profiles (clockwise is positive) at the selected monitoring locations along the foil for σ=2.00 and 0.80, Re=7×10^5, α=8°.

stretching and volumetric expansion/contraction (dilatation) term. In addition to the baroclinic torque, the development of the re-entrant jet, the collapse of the sheet cavity, and the shedding of the cloud cavity are also responsible for the modification of the vorticity distributions. The results also explain the strong correlation between the cavity and vorticity structures. The magnitude of the viscous production term is small as compared to the other terms, and generates vorticity at a solid boundary.

6 Conclusions

Combined numerical and physical analysis are presented for a Clark-Y hydrofoil at a fixed angle of attack of α=8° at Re=7×10^5 for two cavitation numbers representing subcavitating (σ= 2.00) and sheet/cloud cavitating (σ= 0.80) conditions. The primary findings include.

1) The cloud cavity is highly unsteady, and a self-oscillatory behavior of the whole sheet cavitation at cloud cavitating (σ=0.80) are observed. The trailing edge of the cloud cavity exhibits noticeable unsteady characteristics. Associated with the large-scale vortex dynamics, a reentrant flow is induced in the rear, near wall region of cloud cavitation, and the reentrant jet is an important mechanism that triggers the shedding of the cloud cavitation. Both the experimental and simulation results show that the cloud cavity is distorted into a U-shape vapor structure as it moves

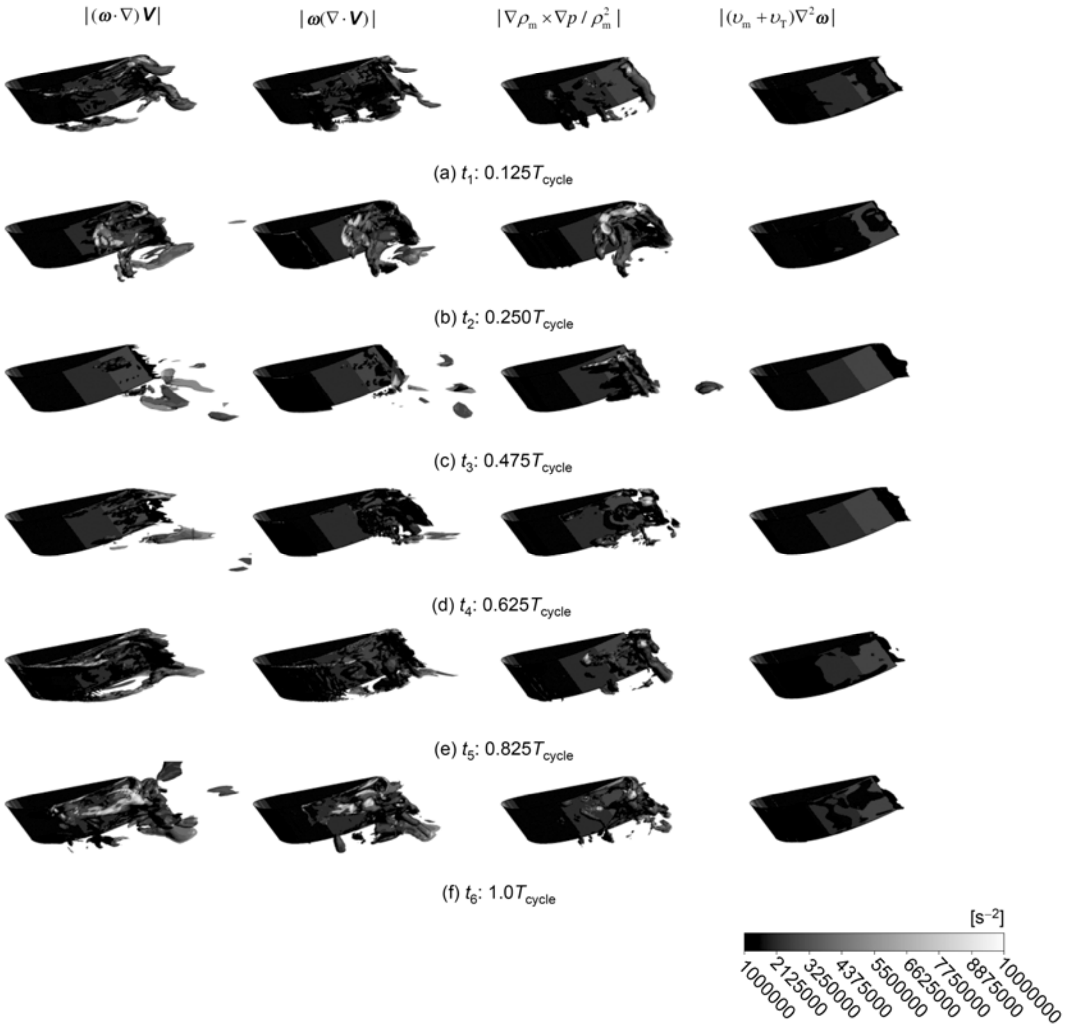

Figure 10 Time evolution of the predicted magnitudes of vortex stretching term, volumetric expansion/contraction (dilatation) term, baroclinic torque and viscoclinic torque at selected times. σ=0.80, Re=7×10^5, α=8°.

downstream, which then splits at its head and finally collapses violently at its legs.

2) The cavitation phenomenon has an important effect on the flow structures due to the significance of the production and modification of the vorticity field by the formation and transformation of the cavity. Compared with subcavitating flows (σ=2.00), large scale of vortical structures can be observed for the cloud cavitating case (σ=0.80).

3) The baroclinic torque is responsible for the generation and modification of vorticity due to shear flow created by the unequal acceleration between the lighter vapor and heavier liquid phases. In addition, the inception, growth, and shedding of cavities modify the vorticity distribution around the foil and in the wake. The interdependency between the cavity and vorticity dynamics is not negligible for the unsteady sheet/cloud cavitating

Overall, this work has contributed to advancing the understanding of flow physics of unsteady cavitating flows. The specific contributions include 1) findings of the unsteady cavitating structures, including the periodic formation, breakup, shedding, and collapse of the sheet/cloud cavities, 2) a better insight in the physical mechanism that governs the dynamics and structures of the sheet/cloud cavitation, 3) quantifying the influence of cavitation on the surrounding flow structures. Additional high quality experiments with detail measurements of the spatial and temporal variation of the vapor fraction and velocity distribution are needed to illuminate the underlying physics and to validate the numerical models. The conventional Reynolds-averaged Navier-Stokes approach based on temporal averaging of the fluctuating terms for homogeneous, incompressible, single phase flows may not be adequent in predicting cavitating flows dominated by transient, large-scale vortices. Higher fidelity simulations via large eddy simulations (LES) and direct numerical simulations (DNS) would better illuminate the flow physics.

More research is also needed to improve interplay between the spatial and temporal variation of the vapor fractions, turbulent velocity fluctuations, and vorticity dynamics around the cavity closure and cavitating wake regions. Research is also needed to improve the understanding of local compressibility effects and associated shock waves on the turbulent flow dynamics. Such research will help significantly improve the understanding and numerical prediction of cavitating flows, which are critical to the hydroelastic stability, fatigue, noise, vibration, and erosion characteristics of hydraulic machineries.

This work was supported by the National Natural Science Foundation of China (Grant Nos. 11172040, 50979004).

1 Batchelor G. An Introduction to Fluid Mechanics. Cambridge: Cambridge University Press, 1967
2 Brennen C E. Cavitation and Bubble Dynamics, Oxford Engineering & Sciences Series 44. Oxford: Oxford University Press, 1995
3 Knapp R T, Daily J W, Hammitt F G. Cavitation. New York: McGraw Hill, 1970
4 Joseph D D. Cavitation in a flowing liquid. Phys Rev E, 1995, 51: 1649–1650
5 Kubota A, Kato H, Yamaguchi H, et al. Unsteady structure measurement of cloud cavitation on a foil section using conditional sampling technique. ASME J Fluids Eng, 1989, 111: 204–210
6 Franc J P. Partial cavity instabilities and re-entrant jet. In: the 4th International Symposium on Cavitation, Paris, France, 2001
7 Kawanami Y, Kato H, Yamauchi H, et al. Mechanism and control of cloud cavitations. ASME J Fluids Eng, 1997, 119: 788–794
8 Kubota A, Kato H, Yamaguchi H. A new modeling of cavitating flows: A numerical study of unsteady cavitation on a hydrofoil section. J Fluid Mech, 1992, 240: 59–96
9 Kunz R F, Boger D A, Stinebring D R, et al. A preconditioned Navier-stokes method for two phase flows with application to cavitation prediction. Comput Fluids Elsevier, 2000, 29: 849–875
10 Merkle C L, Feng J, Buelow P E O. Computational modeling of sheet cavitations. In: Proceedings of third International Symposium on Cavitation. Grenoble, 1998.
11 Morgut M, Nobile E, Bilus I. Comparison of mass transfer models for the numerical prediction of sheet cavitation around a hydrofoil. Int J Multi Flow, 2011, 37: 620–626
12 Chen Y, Heister S D. Modeling hydrodynamic nonequilibrium in cavitating flows. ASME J Fluids Eng, 1996, 118: 172–178
13 Delannoy Y, Kueny J L. Cavity flow prediction based on the Euler equation. ASME Cavit Mult Flow Forum, 1990, 109: 153–158
14 Gopalan S, Kate J. Flow structure and modeling issues in the closure region of attached cavitations. Phys Fluids, 2000, 12: 895–911
15 Reboud J L, Stutz B, Coutier-Delgosha O. Two phase flow structure of cavitation: experiment and modeling of unsteady effects. In: Proceedings of the Third Symposium on Cavitation. Grenoble, 1998
16 Coutier-Delgosha O, Fortes-Patella R, Reboud J L. Evaluation of the turbulence model influence on the numerical simulations of unsteady cavitations. ASME J Fluids Eng, 2003, 125: 38–45
17 Wang G, Ostoja-Starzewski M. Large eddy simulation of a sheet/cloud cavitation on a NACA0015 hydrofoil. Appl Math Modell, 2007, 31: 417–447
18 Johansen S T, Wu J, Shyy W. Filter-based unsteady RANS computations. Int J Heat Fluid Flow, 2004, 25: 10–21
19 Wu J, Wang G, Shyy W. Time-dependent turbulent cavitating flow computations with interfacial transport and filter based models. Int J Numer Methods Fluids, 2005, 49: 739–761
20 Kim S, Brewton S. A multiphase approach to turbulent cavitating flows. In: Proceedings of 27th Symposium on Naval Hydrodynamics. Seoul: Curran Associates, Inc., 2008
21 Laberteaux K R, Ceccio S L. Partial cavity flows. Part 2. Cavities forming on test objects with spanwise variation. J Fluid Mech, 2001, 431: 43–63
22 Dular M, Bachert R, Schaad C, et al. Investigation of a re-entrant jet reflection at an inclined cavity closure line. Eur J Mech B Fluids, 2007, 26: 688–705
23 Saito Y, Takami R, Nakamori I, et al. Numerical analysis of unsteady behavior of cloud cavitation around a NACA0015 foil. Comput Mech, 2007, 40: 85–96
24 Luo X, Ji B, Peng X, et al. Numerical Simulation of cavity shedding from a three-dimensional twisted hydrofoil and induced pressure fluctuation by large-eddy simulation. ASME J Fluids Eng, 2012, 134: 041202
25 Ji B, Luo X, Wu Y, et al. Numerical analysis of unsteady cavitating turbulent flow and shedding horse-shoe vortex structure around a twisted hydrofoil. Int J Multi Flow, 2013, 51:33–43
26 Zwart P, Gerber A, Belamri T. A two-phase flow model for predicting cavitation dynamics. In: the 5th International Conference on Multiphase Flow. Yokohama: Japanese Society for Multiphase Flow, 2004
27 Launder B E, Spalding D B. The numerical computation of turbulent flows. Comput Methods Appl Mech Eng, 1974, 3: 269–289
28 Ducoin A, Huang B, Young Y L. Numerical modeling of unsteady cavitating flows around a stationary hydrofoil. Int J Rotating Mach, Article ID: 215678, 2012
29 Huang B, Ducoin A, Young Y L. Evaluation of cavitation models for prediction of transient cavitating flows around a pitching hydrofoil. In: Proceedings of 8th International Symposium on Cavitation. Singapore: Research Publishing Services, 2012
30 Huang B, Young Y L, Wang G, et al. Combined experimental and computational investigation of unsteady structure of sheet/cloud cavitation. ASME J Fluids Eng, 2012, 135: 071301
31 Huang B, Wang G. Experimental and numerical investigation of unsteady cavitating flows through a 2D hydrofoil. Sci China Tech Sci, 2011, 54: 1801–1812